Large Eddy Simulation of Combustion and Heat Transfer in a Single Element GCH4/GOx Rocket Combustor

D. Maestro, B Cuenot, L. Selle

Flow, Turbulence and Combustion manuscript No.
(will be inserted by the editor)

Large Eddy Simulation of combustion and heat transfer in a single element GCH_4/GOx rocket combustor

D. Maestro[†] · **B. Cuenot**[†] · **L. Selle**[§]

Received: date / Accepted: date

Abstract The single element GCH_4/GOx rocket combustion chamber developed at the Technische Universität München has been computed using Large Eddy Simulation. The aim of this work is to analyze the flow and combustion features at high pressure, with a particular focus on the prediction of wall heat flux, a key point for the development of reusable engines. The impact of the flow and flame, as well as of the model used, on thermal loads is investigated. Longitudinal distribution of wall heat flux, as well as chamber pressure, have been plotted against experimental data, showing a good agreement. The link between the heat released by the flame, the heat losses and the chamber pressure has been explained by performing an energetic balance of the combustion chamber. A thermally chained numerical simulation of the combustor structure has been used to validate the hypothesis used in the LES.

Keywords Large-eddy simulation · GCH_4/GOx combustion · Wall heat transfer · Rocket propulsion

Acknowledgements The authors acknowledge CINES (Centre Informatique National de l'Enseignement Supérieur) of GENCI (Grand Équipement National de Calcul Intensif) for giving access to HPC resources under the allocations A0032B10157 and A0012B07036. The authors extend special thanks to Mariella Celano, Simona Silvestri, Christoph Kirchberger, Gregor Schlieben and Oskar Haidn for providing the test case and insightful discussions.

D. Maestro
Tel.: +33(0)5 61 19 30 89
E-mail: maestro@cerfacs.fr

[†] *CERFACS - 42 Avenue Gaspard Coriolis, 31057 Toulouse Cedex 01, France*
[§] *IMFT, 2 Allée du Professeur Camille Soula, 31400 Toulouse, France*

List of symbols

Roman characters

a	Strain rate	[s^{-1}]
C_p	Heat capacity at constant pressure	[J/(kg · K)]
C_{vd}	Van Driest constant	[-]
d_{Ox}	Oxydizer injector diameter	[m]
D_k	Diffusion coefficient of species k	[m^2/s]
HRR	Cumulative heat release rate	[W]
F	Thickening factor	[-]
$\dot{m}$	Mass flow rate	[kg/s]
O/F	Oxidizer-fuel ratio	[-]
P	Pressure	[Pa]
q_w	Wall heat flux	[W/m^2]
Q_{walls}	Cumulative wall heat flux	[W]
S_{ij}	Deformation tensor	[s^{-1}]
S_L^0	Premixed laminar flame speed	[m/s]
$\mathcal{S}$	Surface	[m^2]
t	Time	[s]
T	Temperature	[K]
u	Velocity	[m/s]
u'_Δ	Velocity fluctuation at LES filter scale	[m/s]
$\mathcal{V}$	Volume	[m^3]
y^+	Wall unit distance	[-]
z	Mixture fraction	[-]
(x, y, z)	Spatial coordinates	[m]

Greek characters

χ	Scalar dissipation rate	[s^{-1}]
δ_L^0	Premixed laminar flame thermal thickness	[m]
δ_L^d	Diffusion flame thickness	[m]
Δ_0	Characteristic mesh size	[m]
Δ_{cell}	Local mesh size	[m]
Δ_e	LES filter size	[m]
ϵ	Turbulence dissipation rate	[m^2/s^3]
γ	Heat capacity ratio	[-]
κ	Von Karman constant	[-]
λ	Thermal conductivity	[W/(m · K)]
μ	Molecular (dynamic) viscosity	[Pa · s]
ν	Kinematic viscosity	[m^2/s]
$\dot{\omega}_T$	Energy source term	[W/m^3]
ρ	Density	[kg/m^3]
σ_{ij}	Stress tensor	[Pa]
τ_w	Wall shear stress	[Pa]
θ	Flame sensor for diffusion flame	[-]
Ξ	Flame wrinkling	[-]

Dimensionless numbers

Da	Damköhler number
Pr	Prandtl number
Sc	Schmidt number

Acronyms

CSP	Computational Single Perturbation
DRG	Directed Relation Graph method
LES	Large Eddy Simulation
NSCBC	Navier-Stokes Characteristic Boundary Conditions
QSS	Quasi-Steady State
RANS	Reynolds Averaged Navier-Stokes
TCI	Turbulence Combustion Interaction
TUM	Technische Universität München

Indices and superscripts

$+$	Superscript of quantities written in wall units
c	Index of a Critical value
g	Index of a Gaseous quantity
Λ	Index of Strain Rate induced quantity
num	Index of Numerical (mesh induced) quantity
Π	Index of Flame Wrinkling induced quantity
ref	Index of Reference quantity
sgs	Index of a Sub-grid-scale quantity
st	Index of a quantity at Stoichiometric equivalence ratio
t	Index of Turbulent quantity
tot	Index of Overall quantity
TCI	Index of TCI model quantity
τ	Index of Friction quantity
w	Index of a quantity located at Wall

1 Introduction

Cost effectiveness has become nowadays a major design constraint for rocket engines. This is due to a shift in the market of access to space from government agencies to private companies, which claim to reduce the cost per kilogram in orbit by at least one order of magnitude. Such an ambitious goal requires a technological breakthrough of the propulsion system, which has to be operated at low cost and be reusable. A major path of evolution for rocket engines has been found to be the substitution of liquid hydrogen by hydrocarbons as fuel. The propellant combination liquid oxygen-liquid hydrogen (LOx/LH_2) has been used for a long time and is commonly used today to propel among others the European launcher Ariane 5. This is thanks to the very high specific impulse of hydrogen, which has however drawbacks in terms of cost of production and handling. Its low density requires large storage tanks, which have moreover to be kept at a very low temperature to maintain the propellant in a liquid state (around 20 K). In addition, hydrogen requires the use of Helium, an expensive and scarce fossil gas, to drain and pressurize.

Among others hydrocarbons, methane characteristics are particularly promising. It offers high specific impulse (compared to kerosene for instance [1]), high density at common tank pressures (around 6 times the density of hydrogen), low pollution and low cost both for production and handling [2]. With the objective of reusable engines, the fuel cooling properties have also become one of the key parameters for the selection of hydrocarbon fuels. Thanks to its high thermal conductivity, specific heat and low viscosity, the heat transfer performance of methane is higher compared to other hydrocarbon fuels. Moreover, in cooling systems, the maximum temperature allowed for coolant-side wall is commonly limited by the coking temperature of the fuel: the typical value for methane is 970 K, higher than propane (700 K) and kerosene (590 K) [3].

Compared to H_2/O_2 combustion, which has been extensively studied, there is a lack of knowledge of CH_4/O_2 combustion at high pressure. Flame and flow behavior, including flame stabilization, temperature stratification as well as gas composition near walls are however key phenomena for a best engine operation. In particular, controlling the wall temperature during operation is a mandatory step to reach the objective of reusable engines. Indeed, life cycle of rocket engines strongly depends on the wall temperature: a difference of 40 K may lead to a life reduction of 50 % of a cryogenic propellant rocket chamber [4]. Thermal loads on the walls, including their unsteady behavior, are consequently required for the design of combustion chambers. In view of the complexity and cost of experiments, numerical simulations are essential to understand the physical phenomena and predict thermal stresses on the chamber walls.

Although different groups performed experimental investigations [5,6], few data are available for combustion of gaseous oxygen and gaseous methane at relevant chamber conditions. In order to provide experimental data specifically suited for numerical simulations, a test campaign has been conducted at the Technische Universität München. In the context of the national research program Transregio SFB/TR-40 on "Technological Foundation for the design of thermally and mechanically high loaded components of Future Space Transportation System" a new combustor rig has been developed and tested. Experimental data has been provided by Celano et al. [7]. The test case has been firstly simulated during the

2015 SFB/TRR 40 Summer Program. A "blind test" was performed by different groups, showing a significant spread in results, compared to the test data [8,9]. Updated results have been presented by Roth et al. [10], Maestro et al. [11] and Müller et al. [12].

Recent results by Maestro et al. [13] showed how the prediction of wall heat flux in a rocket chamber type configuration requires both correct modeling of the flow and flame, including the chemical flame structure, the gas composition and the temperature gradient at walls.

In this paper a full 3D Large Eddy Simulation (LES) with direct integration of methane oxy-combustion chemistry of the experimental setup of Celano et al. [7] is presented. The objective is twofold: (i) investigate the capability of LES to retrieve correct estimations of wall heat flux and chamber pressure evolution and (ii) analyze the flow and flame and their impact on thermal loads. To assess the robustness and reliability of the LES, the impact of the chosen models and parameters is carefully analyzed.

The paper is structured as follows: first, the experimental setup is presented in section 2, then simulation strategy and numerical setup are described in section 3. Flow and flame structures are analyzed in section 4, where quantitative comparisons with measurements are shown. A chained heat conduction simulation of the solid structure is performed in section 5, in order to cross-validate the heat flux estimations. Finally, conclusions and future works are summarized in section 6.

2 Experimental configuration

The configuration (Fig. 1) consists of a 290 mm-long combustion chamber fed

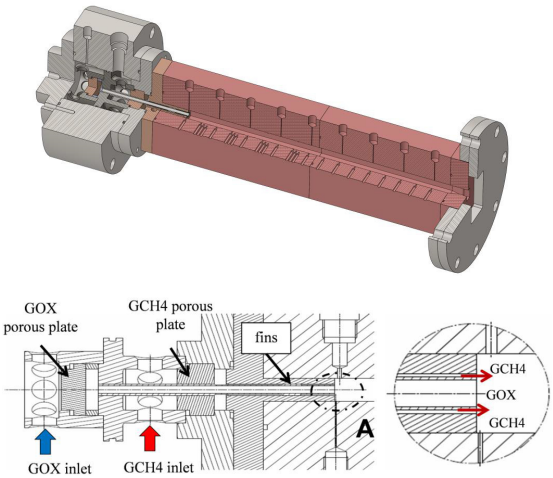

Fig. 1: Single-injector combustion chamber and detail of the injector. Adapted from [14] with permission from M. Celano.

by a single shear coaxial injector, operating at a nominal pressure of 20 bar.

The injector is mounted on an oxygen-free copper combustion chamber with a square cross section (12 × 12 mm) and a nozzle at the exit. The nozzle features a contraction ratio of 2.5, leading to a Mach number in the chamber of 0.24. Combustion chamber and injector characteristics are summarized in Tab. 1.

Combustion chamber		
Chamber length	[mm]	290
Chamber width	[mm]	12
Chamber height	[mm]	12
Throat height	[mm]	4.8
Contraction ratio A_{cc}/A_{th}	[-]	2.5
Injector		
GOx diameter	[mm]	4
GOx post wall thickness	[mm]	0.5
GOx post recess	[mm]	0
GCH_4 outer diameter	[mm]	6
Injector area ratio A_{GCH4}/A_{GOx}	[-]	0.7

Table 1: Characteristic combustion chamber and injector dimensions.

The injector is mounted with no recess on the faceplate providing, thanks to the coaxial configuration, a central core of gaseous oxygen surrounded by high speed gaseous methane. Two porous plates are placed in the oxidizer and fuel manifolds to ensure homogeneous injection conditions in terms of temperature and pressure. The inlet mass flow rates of $\dot{m}_{CH4} = 0.017$ kg/s and $\dot{m}_{O2} = 0.045$ kg/s, are imposed using sonic orifices. This leads to a global oxidizer/fuel ratio $O/F = 2.6$. The injection temperatures of oxygen and methane are of 278 K and 269 K respectively.

The combustion chamber is equipped with pressure transducers, equally spaced on the side wall in order to extract the static pressure distribution $P(x)$ along the chamber axis. This permits a better understanding of the heat release rate distribution and of the complex heat transport processes. Thermocouples have been used in order to quantify the temperature field in the chamber structure. The recorded data have been post-processed in order to reconstruct the wall heat flux evolution along the chamber walls solving the inverse heat conduction problem [15]. Detailed information about the experimental measurement setup can be found in Celano et al. [14, 7, 15]. The chamber is capacitively cooled and therefore the wall chamber temperature increases during the burning experimental time, which is of 3 s. The measured wall temperature in the chamber is averaged over an evaluation time of 0.5 s, centered at 2/3 of the burning time (t_1 in Fig. 2).

3 Simulation setup

3.1 Geometry - Computational domain and mesh characteristics

The computational domain is the full three-dimensional chamber. It starts 1 mm before the faceplate, so that only a small part of the injector is calculated, and extends to the nozzle exit, so that the full nozzle is simulated. The domain is discretized with a hybrid tetrahedral-prism unstructured mesh of about 200×10^6

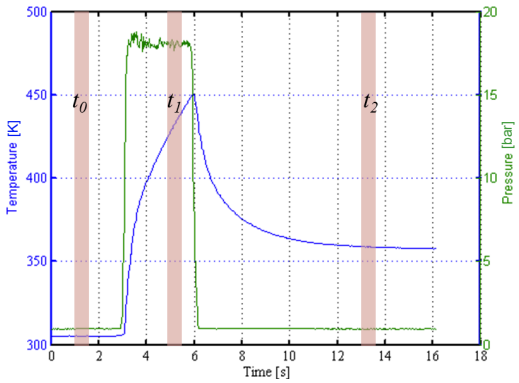

Fig. 2: Typical chamber pressure and thermocouple temperature evolution during a hot run. Reproduced from [14] with permission from M. Celano.

cells. The flame zone refinement has been treated with a particular attention, especially in the post-tip zone, which has been discretized with 20 cells (characteristic mesh size $\Delta_0 = 25$ μm). Ten prism layers have been used to discretize the chamber walls region, leading to an average y^+ value of about 45. A schematic view of the mesh in the near injector region is presented in Fig. 3.

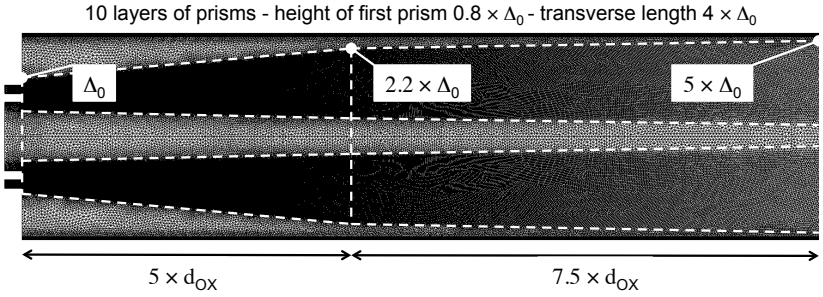

Fig. 3: Longitudinal cut through the mesh near the injector.

3.2 Chemical kinetics

The LES is run with the analytically reduced mechanism developed by Sankaran et al [16] and called here the LU13 mechanism. Analytical mechanisms use a partial equilibrium formulation for some reactions and a quasi-steady-state (QSS) approximation for some species. The QSS approach can be used when the consumption rate of a species is fast compared to its creation rate. This means that the species is very quickly consumed after being produced so that its mass can not significantly change. In this case the net rate of the species is considered equal to zero, its conservation equation is not solved and its concentration is calculated from an analytical formulation instead. The LU13 mechanism has been derived

by Sankaran et al. [16] for air/methane lean premixed combustion using directed relation graph (DRG) [17], sensitivity analysis and computational singular perturbation (CSP) [18] over the GRI-1.2 detailed mechanism [19]. The final skeletal mechanism contains 73 elementary reactions with 17 species. CH_2, $CH_2(S)$, HCO and CH_2OH are identified as QSS species through CSP and their algebraic relations are solved analytically. The remaining 13 species are fully resolved, namely, H_2, H, O, O_2, OH, H_2O, HO_2, CH_3, CH_4, CO, CO_2, CH_2O and N_2.

Mari et al. [20] pointed out that oxy-combustion of methane is very sensitive to the number of species used in the reduced mechanism and that, if they are not sufficient, the equilibrium state of the burnt gases is not correctly retrieved. The kinetic scheme has therefore been validated first on equilibrium calculations and then on 1D premixed and strained counterflow diffusion flames, using representative strain rate values. This has been done using the CANTERA [21] software and a detailed analysis can be found in Maestro et al. [11].

Under experimental conditions, the equilibrium temperature is 3290 K and the burnt gases composition (Tab. 2) is dominated by H_2O and CO, which prevails over CO_2 as a consequence of fuel-rich mixture. It is also visible that a small quantity of O_2 is still present in the reaction products, while CH_4 is completely consumed. The LU13 analytically reduced mechanism recovers very well the correct burnt gases state. The relative error is lower than 0.01% for the temperature and species mass fractions (Tab. 2). For a further validation of the kinetic scheme, 1D premixed

	GRI30	**LU13 [16]**
Temperature [K]	3289.11	3289.14
O_2 mass fraction [-]	5.242e-3	5.243e-3
CH_4 mass fraction [-]	4.328e-10	4.328e-10
CO_2 mass fraction [-]	1.663e-1	1.663e-1
CO mass fraction [-]	3.713e-1	3.713e-1
HO_2 mass fraction [-]	2.196e-5	2.196e-5
H_2O mass fraction [-]	4.037e-1	4.037e-1

Table 2: Equilibrium values: comparison between detailed (GRI30) and reduced (LU13) mechanisms.

flames have been computed to check the value of flame speed and flame thickness. From detailed chemistry calculations, using the experimental temperature and pressure and considering a stoichiometric mixture, these have been found to be 1.4 m/s and 1.7×10^{-5} m, respectively. The flame speed is slightly under-predicted by the reduced mechanism, with a relative error of 15 %. The agreement on the flame thickness is excellent, with a relative error of 3 % for the reduced mechanism.

The behavior of the reduced scheme is also evaluated in the configuration of a strained counter-flow diffusion flame, in order to represent the environment in which the flame develops in the combustion chamber. To vary the strain rate applied to the flame, a series of calculations have been made with different values for the fuel and oxidizer streams velocity. Starting from a very low value, the strain rate is increased up to the value at which extinction occurs. Evolutions of the maximum temperature and maximum heat release rate versus strain rate are plotted in Fig. 4 for the detailed and reduced mechanisms. As expected from theory, an increase in strain rate causes a decrease in maximum temperature, as the result of faster diffusion. Conversely, the maximum heat release rate increases with

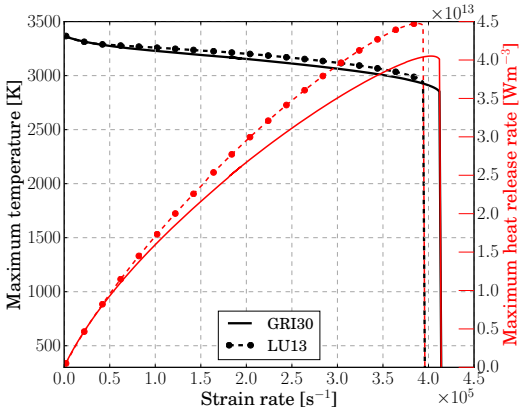

Fig. 4: Strained diffusion flames: evolution with strain rate of maximum temperature (black) and maximum heat release rate (red). Comparison between detailed (GRI30) and reduced (LU13) mechanisms.

increasing strain rate, until extinction suddenly occurs. For both quantities, the LU13 mechanism gives results very close to the detailed mechanism. The extinction strain rate value is slightly different, with the LU13 mechanism underestimating it; however, as it will be detailed later on, the maximum values of resolved strain rate found in the numerical simulations are always lower than 1.2×10^5 s^{-1}, values for which the error of the LU13 mechanism stays very low.

The diffusion flame structures obtained with the two chemical schemes are then compared in the mixture fraction space at a representative strain rate value, $a = 5000$ s^{-1}, in Fig. 5. To evaluate this value, scalar dissipation rate along the

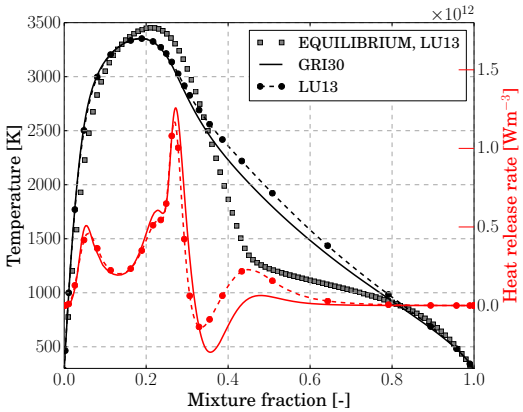

Fig. 5: Strained diffusion flame at $a = 5000$ s^{-1}: profile of temperature (black) and heat release rate (red). Comparison between detailed (GRI30) and reduced (LU13) mechanisms.

stoichiometric surface $\chi_{st} = 2D(\partial z/\partial x_i)^2_{st}$, with z the mixture fraction calculated according to Bilger's [22] definition and D the diffusion coefficient, has been ex-

tracted from the simulation in a representative area of the flow (see Sec. 4.2). Reminding that:

$$\chi_{st} = \frac{a}{\pi} exp(-2[erf^{-1}(1-2z_{st})]^2) \tag{1}$$

where a is the strain rate, and erf is the error function defined as:

$$erf(\eta) = \frac{2}{\sqrt{\pi}} \int_0^{\eta} e^{-x^2} dx \tag{2}$$

one can retrieve the strain rate values in the numerical simulations. A probability distribution function has been extracted in this area and results are presented in Fig. 6: the peak of probability is at a strain rate value of about 5000 s^{-1}, while the maximum value encountered is of about 1.2×10^5 s^{-1}.

The temperature and heat release rate profiles shown in Fig. 5 are well reproduced

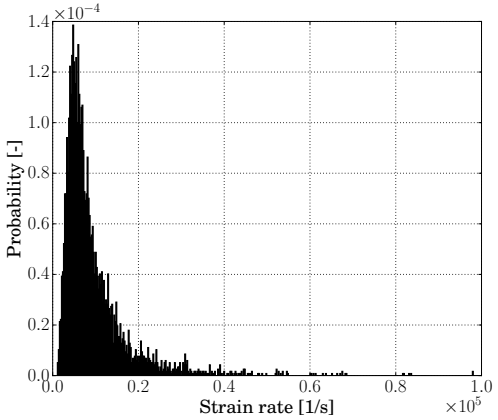

Fig. 6: Probability density function of strain rate in a representative area of the flame (white box in Fig. 9)

by the LU13 mechanism in comparison to GRI30. The temperature profile peaks near the stoichiometric value $z_{st} = 0.2$, where it exhibits a low curvature, linked to the complex, multiple-peaks profile of the heat release rate, which extends over a relatively large range of z. The reduced scheme describes well the complexity of this profile, associated to different reactions located at different values of the mixture fraction. Note that on the rich side the temperature is slightly over-predicted by the LU13 mechanism, due to the lack of some radicals.

The gray symbols in Fig. 5 represent the equilibrium temperature for the whole range of mixture fraction. If equilibrium is almost reached around stoichiometry and on the lean side, denoting fast chemistry, it is far to be the case on the rich side, due to slow recombination reactions in this zone. This justifies the importance of including a direct integration of chemistry rather than using an "infinitely fast" chemistry formulation, which would always stay on the equilibrium line.

3.3 Boundary conditions

The inlet mass flow rates of gaseous oxygen (GOx) and methane (GCH_4), as well as the experimentally measured temperature, have been prescribed at inlet with averaged turbulent velocity profiles, using the NSCBC formulation [23]. At the outlet there is no need to specify any boundary condition, since the flow is expected to be supersonic. The velocity profile prescribed at inlet corresponds to a turbulent flow, coherent with a previous RANS simulation [24]; no additional fluctuations are imposed. The injector walls, as well as the faceplate, post-tip and nozzle walls are treated as adiabatic walls, with a standard law-of-the-wall formalism. Chamber walls are treated as isothermal, with an imposed temperature profile reconstructed from experimental data (Fig. 7). Wall flow in the chamber is

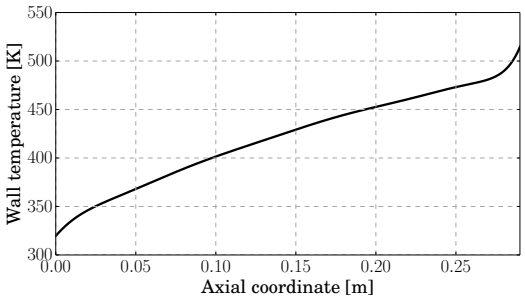

Fig. 7: Imposed temperature along the axial coordinate of the combustion chamber.

modeled with an isothermal wall law, using an improved formulation that couples the velocity and temperature profiles to take into account the interaction between the strong temperature and velocity gradients in the boundary layer. A detailed description of this coupled wall law can be found in the work of Cabrit [25], who demonstrated that for wall bounded flows in which the gases temperature is much higher than the wall temperature ($T_g/T_w > 3$), standard wall laws [26] are not valid anymore.

In standard wall laws characteristic flow scales are used: the friction velocity $u_\tau = \sqrt{\tau_w/\rho_w}$ and the friction distance $y_\tau = \nu_w/u_\tau$, where τ_w is the wall shear stress and ρ_w and ν_w are respectively the density and the kinematic viscosity evaluated at the wall. Wall units are generally introduced: $u^+ = u/u_\tau$ and $y^+ = y/y_\tau$. In the same way it is generally introduced the friction temperature $T_\tau = q_w/(\rho_w C_{p,w} u_\tau)$, obtaining $T^+ = (T_w - T)/T_\tau$. Here q_w denotes the wall heat flux and $C_{p,w}$ the heat capacity evaluated at the wall.

In the coupled wall law the velocity and temperature write (y_c^+ represents the

critical value for the switch between linear and logarithmic laws):

$$y^+ < y_c^+ : u^+ = y^+ \; ; \tag{3}$$

$$T^+ = y^+ \tag{4}$$

$$y^+ > y_c^+ : \frac{2}{\mathrm{Pr}_t B_q}\left(\sqrt{1 - KB_q} - \sqrt{T^+}\right) = \frac{1}{\kappa}\mathrm{ln}y^+ + C_{vd} \; ; \tag{5}$$

$$T^+ = (\mathrm{Pr}y^+)e^{\Gamma} + (\mathrm{Pr}_t u^+ + K)e^{1/\Gamma} \tag{6}$$

with

$$\Gamma = \frac{10^{-2}(\mathrm{Pr}y^+)^4}{1 + 5\mathrm{Pr}^3 y^+} \tag{7}$$

$B_q = T_\tau / T_w$ is the isothermal parameter, $C_{vd} = 5.5$ is the Van Driest constant, $\kappa = 0.41$ is the Von Karman constant and K writes:

$$K = \beta(\mathrm{Pr}) - \mathrm{Pr}_t C_{vd}\left(\frac{\mathrm{Pr}_t}{\kappa} - 2.12\right)(1 - 2\mathrm{ln}(20)) \tag{8}$$

with

$$\beta(\mathrm{Pr}) = (3.85\mathrm{Pr}^{1/3} - 1.3)^2 + 2.12\mathrm{lnPr} \tag{9}$$

In AVBP the switch between the linear and logarithmic laws is done at a critical value $y_c^+ = 11.445$. Using a Van Wijngaarden-Dekker-Brent [27] resolution algorithm, the quantities of interest τ_w (wall shear stress) and q_w (wall heat flux) are retrieved.

Reminding wall temperature of Fig. 7 and the equilibrium temperature of 3290 K, one can calculate values of $T_g/T_w > 5$ in the present case: the use of the coupled model of the wall law is mandatory in order to have a good estimation of the wall quantities. Tests performed with the standard law-of-the-wall confirmed that the resulting error would be unacceptable.

3.4 Numerical setup

The LES is carried using the AVBP solver, developed by CERFACS and IFPEN. It is an unstructured, explicit, compressible code [28,29]. The numerical scheme used is the Lax-Wendroff [30] one, second order in time and space. The sub-grid stress tensor is closed using the Sigma model [31]. Constant turbulent Prandtl number and turbulent Schmidt number (value fixed at 0.7 for both) are used to deduce the thermal and species diffusion terms at the sub-grid level, assuming an eddy-diffusivity approach. A power-law function is used to model the molecular viscosity and constant Schmidt and Prandtl numbers are used for species molecular diffusion and thermal conductivity. Note that preferential diffusion is accounted for as different species Schmidt numbers are used.

$$\mu = \mu_{ref}\left(\frac{T}{T_{ref}}\right)^n \tag{10}$$

$$D_k = \frac{\mu}{\mathrm{Sc}_k} \tag{11}$$

$$\lambda = \frac{\mu C_p}{\mathrm{Pr}} \tag{12}$$

The coefficients in the model have been fitted to the results of the Chapman-Enskog theory [32] with Wilke mixing rules [33], $\mu_{ref} = 1.282 \times 10^{-5}$ Pa $\cdot$ s, $n = 0.703$ and $\mathrm{Pr} = 0.895$. The reference temperature is $T_{ref} = 278$ K and $C_p(T)$ denotes the heat capacity at constant pressure. The parameters have been fitted at a composition corresponding to a mixture fraction $z = 0.7$. This has been evaluated to be the better compromise for wall heat flux evaluations as previous numerical simulations showed that the mixture close to chamber walls is fuel rich. Away from the walls the turbulent transport is assumed to be dominating and thus the error committed is expected to be smaller.

The non-premixed flames found in rocket engines are often modeled with a tabulated flamelet approach [10,12]. In the perspective of computing transient phenomena such as ignition, flame stability or thermo-acoustic instabilities, a direct integration of combustion chemistry is preferred in the present work. This is realized thanks to the thickened flame concept [34] which also models the turbulence/combustion interaction (TCI). Originally derived for premixed flames, it was recently extended by Shum-Kivan [35] to non premixed combustion as briefly presented below. In the case of high Da number, the thickness of a diffusion flame is controlled by the mixture fraction gradient and can be expressed as $D/\sqrt{\chi}$ where χ is the scalar dissipation rate. This means that the simulated flame fits to the resolved flow and scalar dissipation, whatever the LES mesh resolution. This is a significant difference with premixed flames which have their own thickness. For this reason, it is not necessary to further artificially thicken a diffusion flame for issues of numerical stability. However, if the calculation of the flame is numerically stable, the heat release rate is not necessarily estimated correctly. Shum-Kivan [35] demonstrated that the difference between the heat release rate obtained from LES and the exact reference (from DNS in his work) comes from three different effects: the mesh under-resolution, the missing sub-grid scale strain rate and the missing sub-grid scale flame wrinkling. The mesh under-resolution acts like numerical diffusion, causing an increase of the thermal thickness of the flame and an overestimation of the global heat release; the loss in sub-grid scale strain rate and wrinkling cause on the contrary an underestimation of the heat release rate. Following the thickened flame concept, Shum-Kivan [35] proposed to recover the exact heat release rate by a modification of the diffusivity D_{TCI} in the flame zone :

$$D_{TCI} = F_{num} \cdot F_{\Pi} \cdot F_{\Lambda} \cdot D \tag{13}$$

where $F_{num} < 1$ represents the effect of the mesh under-resolution, $F_{\Pi} > 1$ represents the loss in flame wrinkling and $F_{\Lambda} > 1$ represents the loss in strain rate. Contrarily to a premixed flame, where the factor F is strictly > 1 [34], $F_{tot} = F_{num} \cdot F_{\Pi} \cdot F_{\Lambda}$ can be greater or smaller than one for a diffusion flame. This is due to the factor F_{num}, which can be interpreted as the inverse of flame thickening by the grid. To counteract this numerical thickening, a "thinning" factor, i.e., lower than 1, must therefore be applied. In addition, as in premixed flames, a modification of D in the whole domain would modify the mixing of reactants and products outside the reaction zone, which must be avoided. The modification of D is then applied locally in the flame zone by means of a flame sensor. For diffusion flames, it is based on the stoichiometric mixture fraction z_{st} and it reads:

$$\theta = \min(A \times \exp(-B \times (z - z_{st})^2), 1) \tag{14}$$

where A and B are constants which control the steepness and width of the sensor and have been fixed to 4 and 2000, respectively. Tests on laminar flames and also turbulent flames have been performed in order to make sure that the reaction zone is adequately detected while keeping the non-reacting zone unaffected. Finally the diffusivity is modified as follows:

$$D^* = \theta D_{TCI} + (1-\theta)(D + D_t) \tag{15}$$

with D_t the turbulent diffusivity introduced by the sub-grid scale model.

The determination of F_{tot} is a key element in this approach. The development of a generic model to directly and accurately evaluate this coefficient from the numerical solution is beyond the scope of this work and will be the subject of further studies. In this work, simple rules were applied which guarantee an improved TCI description.

The correction coefficient was estimated as $F_{num} = \Delta_0/\Delta_{cell}$, where Δ_0 is the mesh size required to resolve the flame in the whole range of strain rate at the resolved scale and Δ_{cell} is the local characteristic size of the single cell. Figure 6 shows a strain rate with a non-negligible occurrence of $a = 5000$ s^{-1}: at these conditions the flame thickness is found to be of 154 μm and a mesh size of $\Delta_0 = 25$ μm provides 6 points in the flame thickness, which are in general sufficient. Figure 6 also shows that the strain rate may reach up to $a = 1.2 \times 10^5$ s^{-1}, which occurs very rarely. At this strain rate, the diffusion flame thickness is found to be of 34 μm which is close to Δ_0, meaning that this flamelet will be present but not accurately described. However, the low occurrence of this strain rate makes this error acceptable. With $\Delta_0 = 25$ μm, F_{num} is found in the range $0.025 < F_{num} < 1$.

Then, in order to account for sub-grid scale effects the coefficient $F_{sgs} = F_\Lambda \cdot F_\Pi > 1$ has also been applied.

The sub-grid scale strain rate has been here evaluated by calculating the turbulence dissipation

$$\epsilon = 2\nu S_{ij} S_{ij} \tag{16}$$

from the resolved field, with $\nu = \mu/\rho$ the kinematic viscosity and

$$S_{ij} = \frac{1}{2}\left(\frac{\partial u_j}{\partial x_i} + \frac{\partial u_i}{\partial x_j}\right) \tag{17}$$

the deformation tensor. The turbulence dissipation is evaluated in the flame zone, giving $\epsilon \approx 10^6$ m^2/s^3. The sub-grid scale strain rate can be evaluated, under the hypothesis of homogeneous isotropic turbulence:

$$a_{sgs} = \sqrt{\epsilon/\nu} \approx 10^5 \text{ s}^{-1} \tag{18}$$

being $\nu \approx 5 \times 10^{-5}$ m^2/s in the flame zone. This value is higher than the value of the resolved strain rate calculated in section 3.2, i.e. $\approx 10^3 - 10^4$ s^{-1} and could lead to an increase in the total heat release rate. It is however known [36] that, in order to increase the flame heat release rate, turbulent structures have to perturb the flame for a sufficient amount of time. The highest sub-scale strain rates are generally associated to the smallest vortical structures and small vortices are rapidly dissipated. Considering this, together with the fact that an increase of one order of magnitude in strain rate leads to an increase in heat release rate

lower by far from one order of magnitude (see Fig. 4), we make the assumption that $F_\Lambda \approx 1$ as a first step.

Regarding F_Π, it has been calculated as an efficiency function following the model of Charlette et al. [37]. This model evaluates the loss in wrinkling caused by the artificial thickening of the flame by the mesh. To do that, it compares the flame wrinkling Ξ of the unthickened and mesh-thickened flames. It writes:

$$F_\Pi = \frac{\Xi(\delta_L^0)}{\Xi(\Delta_{cell})} \tag{19}$$

where δ_L^0 is the unthickened flame thickness.
The efficiency function relies on the assumption of equilibrium between turbulence and sub-grid scale flame surface. The evaluation of velocity fluctuations at the LES filter scale u'_Δ is estimated by an operator based on the rotational of the velocity to remove the dilatation contribution [38]. $\Xi(\Delta_{cell})$ is directly known from the LES solution. In premixed flames, $\Xi(\delta_L^0)$ is evaluated as follows:

$$\Xi(\delta_L^0) = \left(1 + \min\left[\frac{\Delta_e}{\delta_L^0}, \Gamma\left(\frac{\Delta_e}{\delta_L^0}, \frac{u'_\Delta}{S_L^0}, \mathrm{Re}_{\Delta_e}\right)\frac{u'_\Delta}{S_L^0}\right]\right)^\beta \tag{20}$$

where $\beta = 0.5$ is a model parameter, S_L^0 and δ_L^0 are the laminar premixed speed and thickness, Δ_e is the LES filter size and Re_{Δ_e} is the flame Reynolds number evaluated at the filter size,

$$\mathrm{Re}_{\Delta_e} = 4\frac{\Delta_e}{\delta_L^0}\frac{u'_\Delta}{S_L^0}. \tag{21}$$

This expression for the flame wrinkling can be adapted to diffusion flames, interpreting S_L^0 and δ_L^0 as the consumption rate and thickness of a diffusion flame under the effect of the sub-grid scale strain rate a_{sgs}. The efficiency function becomes:

$$\Xi(\delta_L^d) = \left(1 + \min\left[\frac{\Delta_e}{\delta_L^d}, \Gamma\left(\frac{\Delta_e}{\delta_L^d}, \frac{u'_\Delta}{\delta_L^d a_{sgs}}, \mathrm{Re}_{\Delta_e}\right)\frac{u'_\Delta}{\delta_L^d a_{sgs}}\right]\right)^\beta \tag{22}$$

detoting with δ_L^d the sub-scale diffusion flame thickness.
The characteristic time associated to the diffusion flame is $\tau_d = 1/a_{sgs} \approx 10^{-5}$ s. It is noticeable how this is close to the characteristic time of a stoichiometric premixed flame at the experimental pressure and temperature, i.e. $\tau_p = \delta_L^0/S_L^0 \approx 10^{-5}$ s, where $S_L^0 = 1.4$ m/s and $\delta_L^0 = 1.7 \times 10^{-5}$ m (see section 3.2).

The values of F_{sgs} predicted by this model are in the range $1 < F_{sgs} < 8$. This leads to an overall $0.2 < F_{tot} = F_{num} \cdot F_{sgs} < 1$. This is coherent with the results of Shum-Kivan [35].

Fields of F_{num}, F_{sgs} and F_{tot} can be seen in Fig. 8. It can be noticed how F_{num} is equal to one in the zone close to the injector lip and then decreases as the mesh is coarsened.

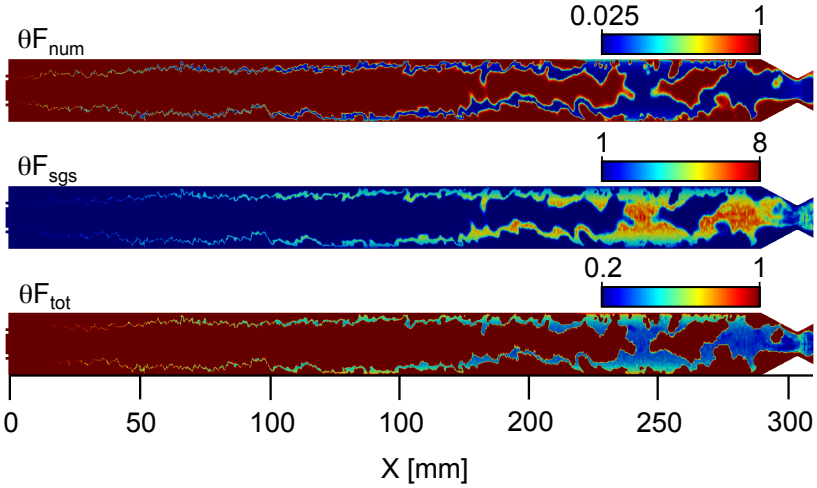

Fig. 8: Fields of F_{num} (top), F_{sgs} (middle) and F_{tot} (bottom), when filtered using the sensor θ. View is stretched by a factor 2 in transverse direction for visualization reasons.

4 Results and discussion

Results of the LES are presented in this section, which begins with an overview of the near-injector flow. An analysis of the flame features follows, with a qualitative and quantitative description of the GCH_4/GOx flame structure and dynamics. A comparison with OH^* chemiluminescence from the experiment is shown. Finally, the axial pressure evolution and the wall heat flux are compared to the experimental data and an energy balance is presented to explain these results.

4.1 Near injector flow field

Figure 9 shows instantaneous and averaged fields of temperature. The flame anchors in the wake of the splitter, where a stable recirculation zone is observed between the cold fuel and oxidizer inflows. The flame then progressively thickens under the effect of turbulence which destabilizes, stretches and wrinkles it. The instantaneous field, along with an analysis of streamlines, shows how the flame is strongly stretched and tends to stay thin in the zone close to the injector. Further downstream, where the strain rate is lower, the thermal expansion of the burnt gases starts to act in the radial direction. This thickens the reaction zone and pushes the cold flow of methane towards the wall, closing the recirculation zone at nearly 14 mm. The recirculation zone is filled by a mixture of fresh methane and burnt gases pockets which detach from the flame and move backward. this is shown in Fig. 10, where an instantaneous field of CH_4 and CO mixture fraction is presented.

A time averaged flow field of OH mass fraction, integrated along the line-of-sight is shown in Fig. 11 and compared to a visualization of the OH^* chemiluminescence from the experiment [39], in the same area near the injector. As quantitative

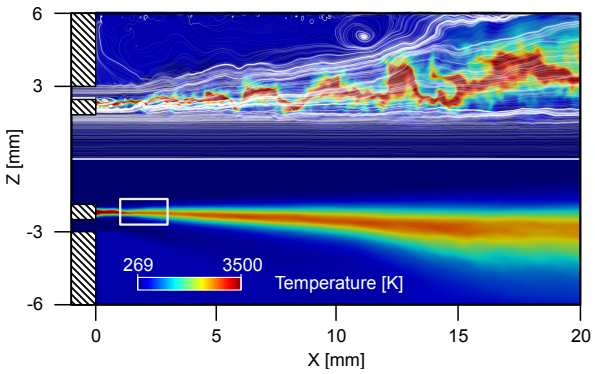

Fig. 9: Temperature field on a longitudinal cut in the near-injector zone. Top: instantaneous field, streamlines. Bottom: temporally averaged field.

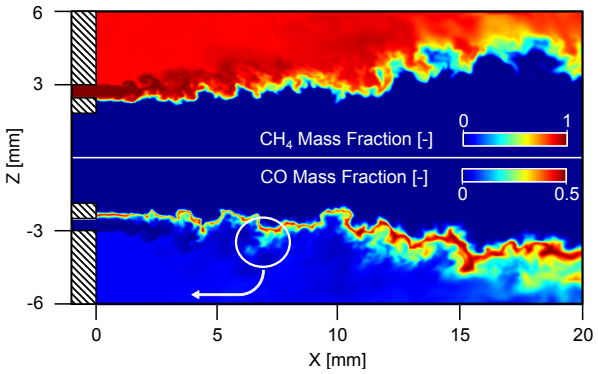

Fig. 10: Top: instantaneous field of CH_4 mass fraction. Bottom: instantaneous field of CO mass fraction.

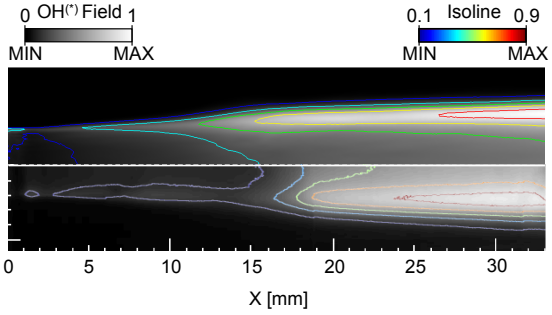

Fig. 11: Top: time averaged field of OH mass fraction from the LES. Bottom: OH^* field from experiment [39].

data are not available, fields have been normalized by their maximum value. The contours have been taken between 10% and 90% of the maximum value. Results show a good qualitative agreement in flame shape and stabilization. Experimental

visualization shows that the light emission is weak up to a distance of 4 to 5 GOx injector diameters, then the flame becomes suddenly brighter. The same behavior is retrieved by the numerical simulation, only slightly earlier. This sudden increase of OH coincides with the flame thickening at an axial coordinate of 15 to 20 mm, corresponding to the end of the recirculation zone.

Note that the species OH^* is not present in the numerical simulation and that OH distribution may differ from OH^*.

4.2 Flame structure

Figure 12 shows an instantaneous field of mixture fraction in the whole chamber. The mixture fraction is calculated calculated following Bilger's definition [22]. The

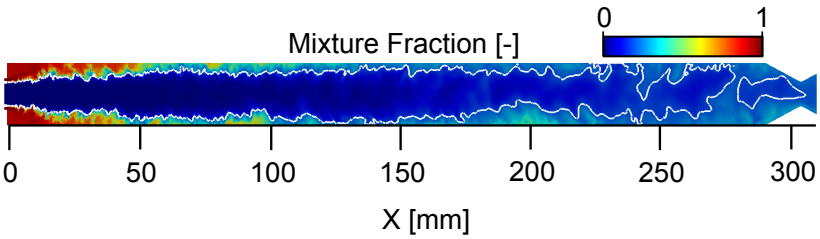

Fig. 12: Field of mixture fraction in a plane perpendicular to injection. White line: isoline of stoichiometric mixture fraction. View is stretched by a factor of 2 in the transverse direction for better visualization.

isoline of stoichiometric mixture fraction (white line) is taken as an indicator of the flame position since the flame burns in a diffusion regime. The flame closes between x = 250 mm and x = 290 mm, where pockets start to detach and exit the combustion chamber, denoting an intermittent incomplete combustion. The flame mostly stays away from the walls, and flame-wall interaction occurs rarely.

The mean flame shape is presented in Fig. 13, top and middle, where time averaged fields of temperature and mixture fraction on a longitudinal cut are shown. The isoline of stoichiometric mixture fraction marks the average position of the flame. The mean flame is attached to the injector lip, expanding radially with a maximum radial position located at about x = 150 mm and closing around x = 280 mm, just upstream the chamber end.
Figure 13, bottom, shows an averaged field of methane mass fraction. It is visible that fuel accumulates along the walls. It is also visible that a thermal boundary layer is formed due to the joint effects of heat losses, induced by the constant-temperature boundary condition, and the presence of a layer of cold methane near the walls. The thermal boundary layer is less and less visible downstream due to the preferential concentration of methane at the edges, as it will be shown later. A thin layer is still present but is not easily visible with the color scale used here.

In order to confirm that the combustion regime is indeed diffusion, the flame structure in the 3D simulation has been compared to 1D counterflow diffusion flames. Values for the 3D simulation have been collected in the vicinity of the injector, between 1 and 3 mm downstream the injector tip, in a cylinder around

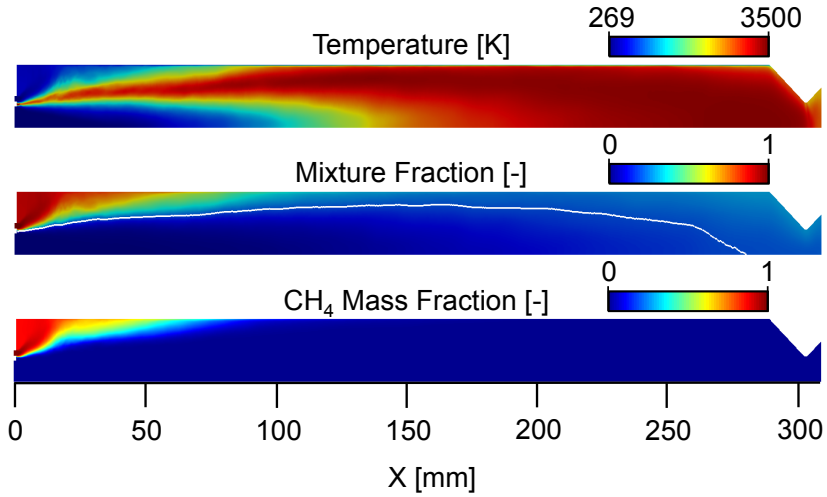

Fig. 13: Longitudinal cut of mean flow fields, stretched by a factor of 4 in transverse direction for better visualization. Top: temperature. Middle: mixture fraction (white line: stoichiometric mixture fraction). Bottom: methane mass fraction.

the flame (white box in Fig. 9). The 1D flame computation has been performed with the Cantera software [21] at the most probable and maximum values of strain rate found in this zone, i.e. $a = 5000$ 1/s and $a = 120000$ 1/s. Results are reported in Fig. 14. A classical diffusion flame structure at strain rate far from extinction

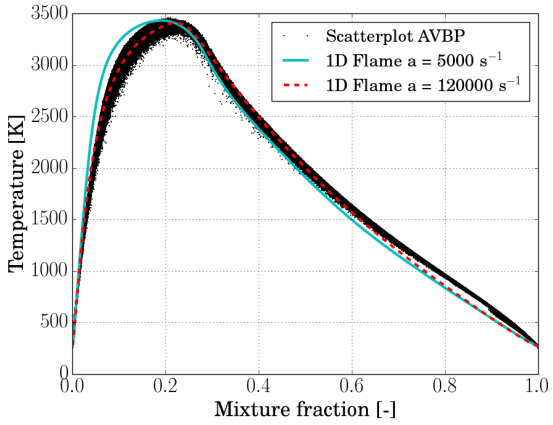

Fig. 14: Scatterplots of temperature vs mixture fraction in the near injection zone, with superimposed curve for a 1D counterflow diffusion flame at two characteristic scalar dissipation rate values.

can be identified. The LES simulation exhibits some dispersion, due to the range of resolved strain rates. Note that the maximum flame temperature is reached and that there is no evidence of heat losses on the flame structure. To illustrate the

3D shape of the flame, Fig. 15 shows transverse cuts of the instantaneous and averaged fields of temperature and methane mass fraction.

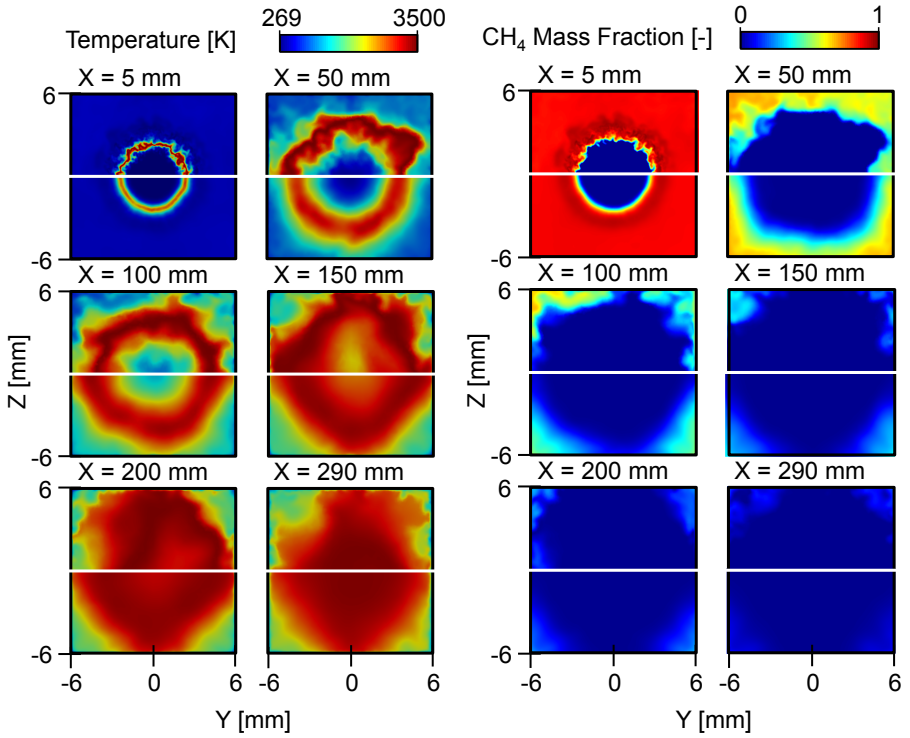

Fig. 15: Transverse cuts of instantaneous (top) and time averaged (bottom) flow fields. Left: temperature, right: methane mass fraction.

In the near injection region, the flame shape is imposed by the injector geometry, leading to a cylindrical flame. Further downstream, the flow field is dominated by the turbulent mixing and the flame shape tends to adapt to the square section of the chamber, resembling to an octogon.

Fields of methane mass fraction on transverse cuts show that the edges of the chamber are filled with CH_4, and remain significantly colder than the central region of the chamber walls. This has a noticeable impact on the circumferential distribution of the heat flux at walls, as shown in Sec. 4.3.

4.3 Quantitative comparison with experimental data

Available experimental data are the axial pressure distribution, indicating the burning intensity, and the heat flux at the chamber walls. The time-averaged pressure distribution along the chamber axis shown in Fig. 16. The profile extracted from measurements shows a fast pressure increase close to the injector, followed by a constant and relatively slow pressure decrease. The pressure difference between

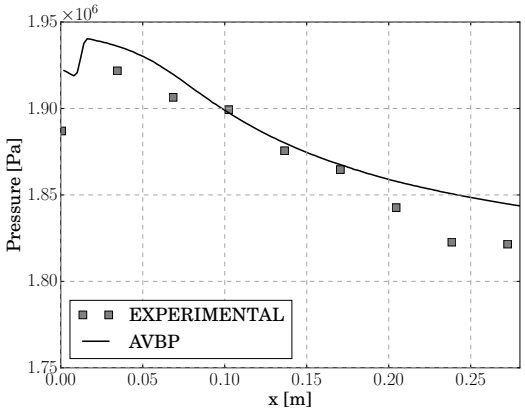

Fig. 16: Time averaged axial pressure evolution.

the two measurement positions at the end of the chamber is nearly zero, indicating the end of the combustion process. The comparison with LES shows that the overall pressure level is quite well predicted, with a slight overestimation. In the first half of the chamber, the decrease in pressure is slightly too fast in the LES, denoting a higher heat release rate than in the experiment. However, close to the end of the chamber, the pressure slope decreases, indicating a reduction in heat release and the end of combustion, consistently with the experiment. This is also in agreement with the flame closure at nearly two thirds of the chamber observed in Fig. 12. The pressure level reached at the exit of the combustion chamber is higher than in the experiment. This is the result of lower heat losses at walls in this zone which are now analyzed.

The evolution of the heat flux at walls has been experimentally obtained using the thermocouples temperatures recorded during the hot fire tests. Celano et al. [7] reconstructed the wall heat flux by solving an inverse heat conduction problem. The main assumption of these calculations is that the heat flux is constant in the circumferential direction of the chamber. In order to compare the LES data with the experimental heat flux profile, the numerical data have been therefore circumferentially averaged.

Results are presented in Fig. 17 (top). Experimental data show a local maximum of heat flux in the near injection region, as a result of the recirculation zone. Downstream the heat flux increases with a fairly constant rate, reaching the highest heat load of 5.33 MW/m^2 at the end of the chamber. The numerical simulation predicts fairly well the axial evolution of the wall heat flux, denoting a correct prediction of the flow and flame dynamics. However the values are slightly underestimated for axial positions greater than 120 mm. Possible causes leading to these differences will be discussed in the following.

In order to verify the assumption of constant heat flux in the circumferential direction, Fig. 17 (bottom) compares the heat flux along the center of the chamber wall (CC in the following) and along the chamber edge (CE in the following). Results show significant differences due to geometrical effects of a cylindrical flame in a square section chamber, highlighted in Fig. 15. The preferential convection of fresh methane towards the CE leads to a thicker thermal layer in this zone and

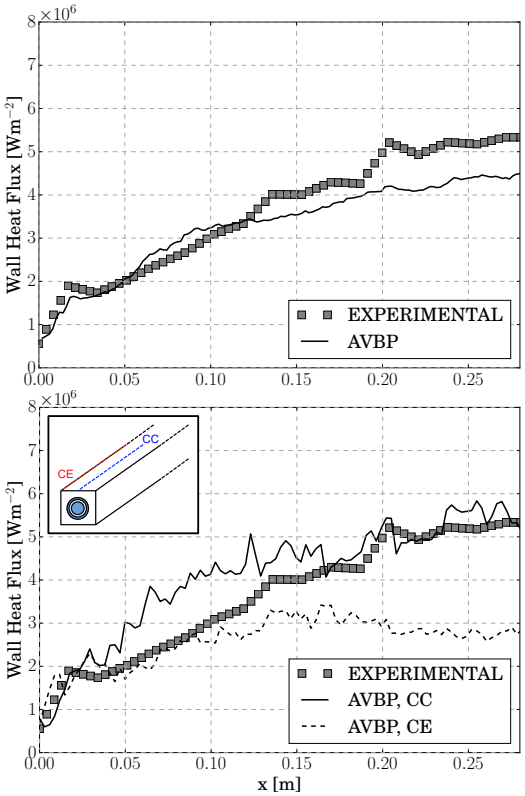

Fig. 17: Top: circumferentially and time averaged axial profiles of heat flux at walls. Bottom: circumferentially and time averaged axial profile of wall heat flux at the chamber center and edge.

therefore to a lower heat flux. On the contrary, at the CC, the hot gases are closer to the walls, leading to a higher heat flux. Only very close to the injection plane, the heat flux is higher at CE than at CC. This is also due to the chamber shape, combined to the presence of the corner recirculation zone. Fig. 18 represents the wall flow in the near injection region: a near wall temperature field (gas temperature in wall cells) is shown and the mean flow motion is schematized. The CE are further away than the CC from the methane injector, leading to corner recirculation zones which extend further upstream. This results in a larger area in which hot gases are brought back from the flame to the CE in comparison to the CC in which the fresh methane rapidly touches the walls and is convected downstream. In order to further investigate the impact of this non-uniformity, a chained thermal conduction simulation, in which the results of the LES are used as boundary conditions for a thermal conduction simulation, is presented in section 5.

Three possible reasons for the under-estimation of the wall heat flux in the second half of the combustion chamber have been identified. First, the combustion model coefficients have been set by using simple rules. This can lead to a slightly different flame shape (different length and/or radial expansion) and to an inaccurate prediction of the heat flux at walls. This should not have a leading order

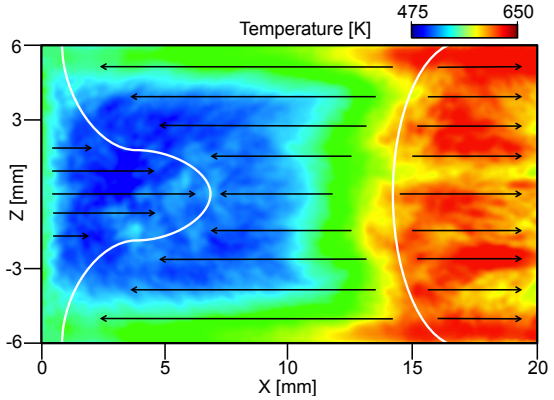

Fig. 18: Schematic of the wall flow in the near injection region. White lines: representation of the zero axial velocity isolines. Black arrows: mean flow direction.

impact in the second half of the chamber, but can have an impact in the first half, changing the overall heat release distribution in the combustion chamber. Second, the power-law function used for the molecular viscosity and the Prandtl number used for the thermal conductivity have been fitted for a fuel rich mixture ($z = 0.7$). This value is acceptable in the first half of the chamber, while in the second half a local mixture fraction of $z = 0.2 - 0.4$ is often found at walls. This could generate an error in the evaluation of the wall heat flux, which can be underestimated of around $5 - 10$ %. Third, an influence of the sub-grid scale model on the heat fluxes is found. The Sigma model [31] is used here because of its very good properties for shear flows, which permit to avoid a large amount of turbulent viscosity and dissipation in the flame. However, it has naturally an asymptotic behavior at solid boundaries: for this reason the turbulent viscosity in zones really close to the walls is very small. This is correct in a case where the boundary layers are resolved, but could lead to errors using wall laws, where the first node off walls is still in the turbulent region. With wall laws it could be better to use models like Smagorinsky [40], in which no damping for walls is present. On the contrary, this kind of model is known to be too dissipative [41] in the flame zone. In order to check the influence of the sub-grid scale model, an additional LES with the Smagorinsky model has been performed. A leading order effect of the sub-grid scale model on the wall heat flux has been found, confirming what already observed by Potier [42]. The wall heat flux estimated using the Smagorinsky model is up to 50 % higher than the one estimated using the Sigma one, as shown in Fig. 19.

4.4 Energy balance

In order to highlight the strong coupling between the heat released by the flame, the heat losses at walls and the pressure evolution in the chamber, a simplified energy balance has been performed. An equation for the conservation of pressure can be obtained from the conservation of sensible energy e_s. The equation for local

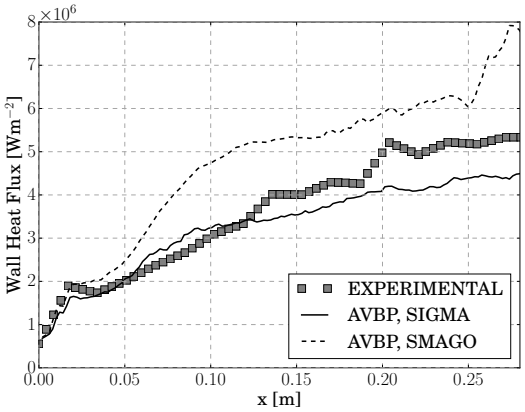

Fig. 19: Circumferentially and time averaged axial profiles of heat flux at walls. Comparison between the Sigma [31] and Smagorinsky [40] sub-grid-scale models.

conservation of pressure writes [43]:

$$\begin{aligned} &\frac{\partial}{\partial t}\left[\frac{1}{\gamma-1}P-\rho C_pT_0\right]+\frac{\partial}{\partial x_i}\left[\frac{1}{\gamma-1}Pu_i-\rho C_pu_iT_0\right]= \\ &=\dot{\omega}_T+\frac{\partial}{\partial x_i}\left(\lambda\frac{\partial T}{\partial x_i}\right)+\sigma_{ij}\frac{\partial u_i}{\partial x_i}+\dot{Q}+f_{vol} \end{aligned} \tag{23}$$

We make now the following assumptions:

- negligible contribution of viscous stresses:

$$\sigma_{i,j}\frac{\partial u_i}{\partial x_i}\approx 0 \tag{24}$$

- no heat source term other than the flame:

$$\dot{Q}=0 \tag{25}$$

- no external volumetric forces:

$$f_{vol}=0 \tag{26}$$

- the energy balance is applied to a time averaged field which is considered to correspond to a steady state solution of the flow:

$$\frac{\partial}{\partial t}\left[\frac{1}{\gamma-1}P-\rho C_pT_0\right]=0 \tag{27}$$

- reference temperature $T_0 = 0$ K (as in AVBP):

$$\rho C_pu_iT_0=0 \tag{28}$$

- constant γ. The value chosen ($\gamma = 1.2026$) is the one which allows to retrieve the correct pressure at the exit of the chamber, so that the pressure evolution can be correctly evaluated.

The equation for the local conservation of pressure then becomes:

$$\frac{1}{\gamma-1}\frac{\partial}{\partial x_i}(Pu_i) = \dot{\omega}_T + \frac{\partial}{\partial x_i}\left(\lambda\frac{\partial T}{\partial x_i}\right) \tag{29}$$

Considering the mean values on a transverse cut of the combustion chamber, we can define a reference state at x = 0 mm where $u = u_0$ and $P = P_0$. Starting from this point, by means of successive integration on a control volume of fluid enclosed between the chamber walls, the reference cut plane and successive planes at growing axial positions x = x′, a 1-D axial evolution of the quantity of interest can be written. Integrating on a control volume $\mathcal{V} = \mathcal{S}\cdot(x' - x_0)$, with $\mathcal{S}$ the cross section of the combustion chamber, it writes:

$$\begin{aligned}\frac{1}{\gamma-1}\iiint_{\mathcal{V}}\frac{\partial}{\partial x}(Pu)d\mathcal{V} &= \frac{1}{\gamma-1}\iint_{\mathcal{S}}\left(\int_{x_0}^{x'}\frac{\partial}{\partial x}(Pu)dx'\right)d\mathcal{S}\\ &= \frac{\mathcal{S}}{\gamma-1}[u_{x'}P_{x'} - u_0P_0]\end{aligned} \tag{30}$$

$$\iiint_{\mathcal{V}}\dot{\omega}_T d\mathcal{V} = [HRR]_{\mathcal{V}} \tag{31}$$

$$\iiint_{\mathcal{V}}\frac{\partial}{\partial x}\left(\lambda\frac{\partial T}{\partial x}\right) = \iint_{\delta\mathcal{V}}\lambda\overrightarrow{\text{grad}}(T)\overrightarrow{dS} = [Q_{walls}]_{\delta\mathcal{V}} \tag{32}$$

Finally, the theoretical evolution of the chamber pressure is obtained:

$$\boxed{\bar{P}(x) = \frac{1}{\bar{u}(x)}\left[u_0P_0 + \frac{\mathcal{S}}{\gamma-1}(HRR(x) + Q_{walls}(x))\right]} \tag{33}$$

Equation 33 shows that the static pressure evolution along the axial distance is controlled by three terms: the heat release rate, the heat losses and the mean velocity. The axial evolution of the quantities of interest is shown in Fig. 20. The black curve represents the evolution of the integrated heat release rate, which increases linearly in the first third of the chamber. Combustion slows then down and the curve slope decreases, with an asymptotic behavior to becoming constant at the end of the chamber. At the exit of the chamber the slope is not zero, denoting incomplete combustion. This is coherent with the presence of pockets of burning gases which exit the combustion chamber, as shown in Fig. 12. The axial evolution of the heat losses at walls is plotted with a dot-dash line. After a first zone in which the increase is really slow (up to x = 70 mm), the losses grow in a quasi-linear way.

The total amount of power released by the flame is of 397 kW. The heat power lost at wall is of 42 kW, i.e. 10.6 % of the flame power.

Using Eq. 33, the theoretical evolution of pressure can be plotted as a function of the evolution of the above-mentioned quantities and of the axial velocity (Fig. 20, bottom): the result is in quite good agreement with the actual pressure evolution in the combustion chamber. After a first peak caused by the end of the recirculation zone, the pressure decreases as we move downstream due to the acceleration of the gases.

Quantitatively the pressure curve obtained using the energy equation is slightly different from the one effectively extracted from the numerical simulation. This

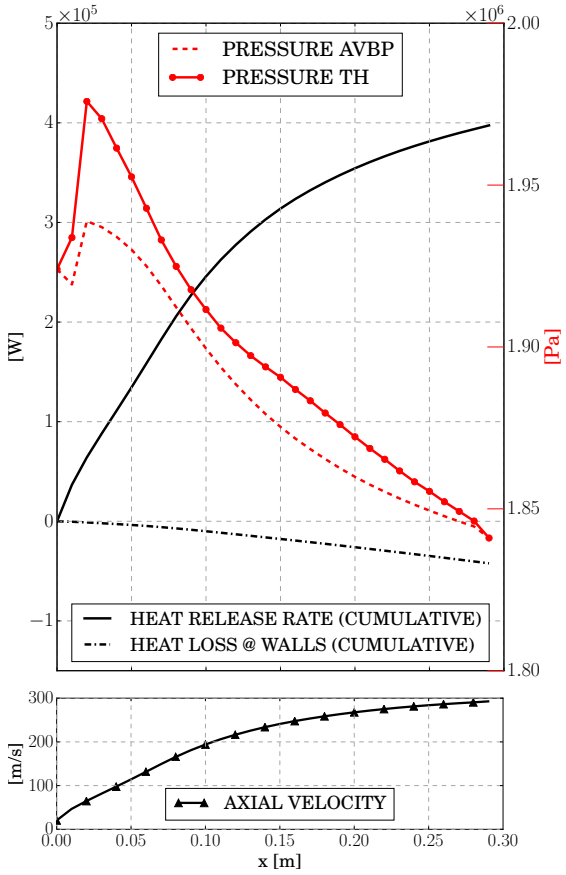

Fig. 20: Energy balance of the combustion chamber. Top: axial evolution of integrated heat release rate (black), heat fluxes at walls (dot-dashed), chamber pressure (dashed, red) and theoretical chamber pressure from Eq. 33 (red, dots). Bottom: evolution of the axial velocity in the combustion chamber.

is due to the strong assumptions made during its derivation. Particularly, the assumption of constant γ has been found to strongly influence the results.

The effects of heat losses on the chamber pressure evolution can now be quantified. Especially, it can be analyzed if the difference found between the LES and the experiment in heat fluxes and pressure curves can be linked. The cumulative heat losses at walls from the experiment have been calculated, resulting in a total heat power lost at walls of around 51 kW, i.e., 21.5% higher than than in LES. Using the LES heat release rate and axial velocity profiles, Eq. 33 can be used to compute the theoretical pressure evolution associated to the experimental heat losses at walls. Results are plotted in Fig. 21.

The heat losses at walls have a clear effect on the pressure evolution: starting from an axial coordinate of x = 120 mm, the theoretical chamber pressure takes lower values when calculated using the experimental heat losses curve rather than the LES ones. Therefore it is clear that the over-estimation of the chamber pressure

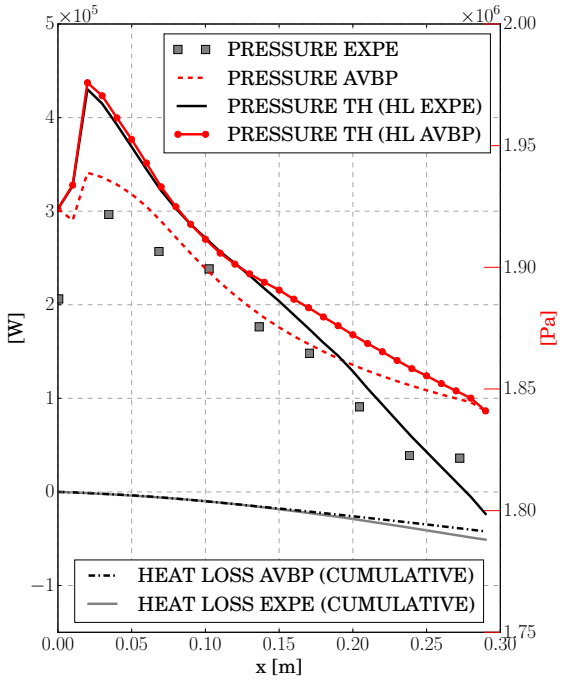

Fig. 21: Energetic balance of the combustion chamber. Axial evolution of experimental pressure (square symbols), LES chamber pressure (dashed, red), theoretical chamber pressure from Eq. 33 using the LES heat fluxes (red, dots), theoretical chamber pressure from Eq. 33 using the experimental heat fluxes (black).

in the LES is linked to the under-estimation of heat fluxes in the downstream part of the combustor. The remaining slight pressure difference is attributed to the heat release rate distribution and subsequent flow acceleration.

5 Thermally chained numerical simulation

As mentioned before, the hypothesis of circumferentially constant heat flux at walls is not perfectly valid. To investigate the associated errors, the calculation of the heat conduction in the combustion chamber walls is performed, starting from the wall heat fluxes provided by the LES. This will provide the temperature field inside the combustion chamber walls, to be compared directly to values recorded by thermocouples during the test campaign.

The thermal simulation has been performed by means of the AVTP solver, dedicated to conduction in solids. AVTP solves the time-dependent temperature diffusion equation, where the heat diffusion follows Fourier's law [44]. The solid solver can take into account local changes of heat capacity and conductivity with temperature. However these variations were not known in the present case and the thermal properties were kept constant. The second-order Galerkin diffusion scheme [45] for spatial discretization is derived from the AVBP solver. Time integration is achieved either with an explicit or an implicit first order forward Euler

scheme. The implicit system, which has been used in the present study, is solved with a parallel matrix free conjugate gradient method [46].

The whole chamber structure has been simulated, starting from 29 mm before the faceplate until the end of the nozzle, and has been discretized by means of a fully tetrahedral unstructured mesh of about 50×10^6 cells. An illustration of the mesh characteristics can be seen in Fig. 22. The mesh is very well refined at

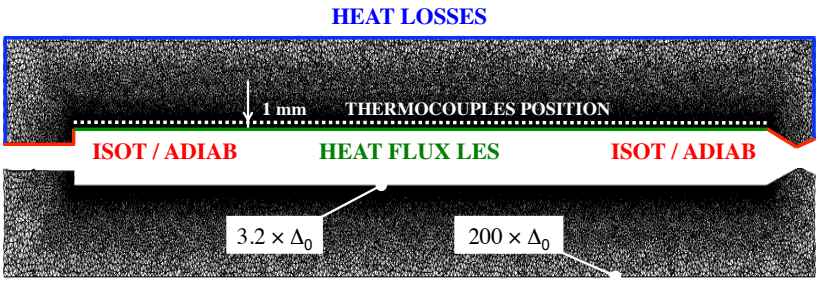

Fig. 22: Longitudinal cut through the mesh (view stretched by a factor 4 in transverse direction) and boundary conditions for the AVTP simulation.

chamber walls, where cells slightly smaller than the respective ones on the fluid side have been used in order to avoid interpolation problems. The cells are then coarsened until the external walls of the chamber.

The structure material is oxygen-free copper (Cu-HCP). The material constants used are in accordance with [47] and have been set as: density $\rho = 8940$ kg/m^3, heat capacity $C_p = 393$ J/(kg $\cdot$ K) and thermal conductivity $\lambda = 385$ W/(m $\cdot$ K). The computational domain has been initialized with a constant temperature of 290 K and the following boundary conditions have been used:

- Inner chamber walls: imposed heat fluxes (constant in time and variable in space) from the LES with the Sigma sub-grid-scale model. As an illustration, the time-averaged flux on one chamber wall at an axial coordinate x = 120 mm is presented in Fig. 23. Although the profile clearly lacks convergence, it gives a correct order of magnitude. It is assumed that steady heat fluxes are quickly reached after ignition and so the heating of the structure during the start-up is neglected. Consider also that as soon as the pressure in the chamber reaches its operating value, the combustion process does not change anymore, this is coherent with the experimental conditions described in Fig. 2. The major assumption is here the constant wall temperatures used in LES (corresponding to the ones measured at 2/3 of the burning time). This could be avoided by performing a fully AVBP-AVTP coupled simulation and may be the subject of further studies. This kind of simulation would be however very CPU expensive.
- Faceplate and external GCH_4 injector wall: conditions on these walls are unknown so that two extreme cases have been performed. In the first case the walls have been both fixed to the experimental chamber wall temperature at the faceplate axial coordinate (ISOT). In the second case an adiabatic condition has been assumed (ADIAB).

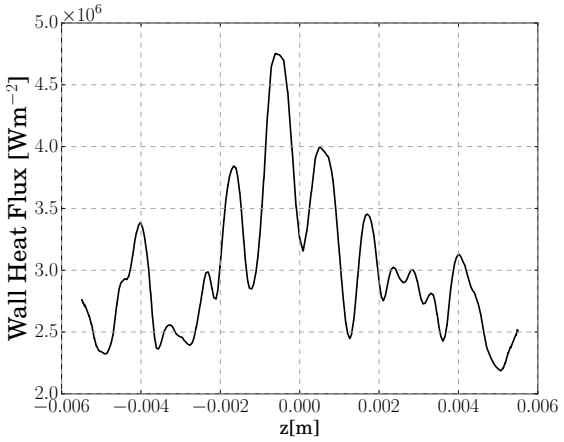

Fig. 23: Circumferential distribution of the wall heat flux on a cut at an axial coordinate x = 120 mm.

- Nozzle walls: here too, two cases have been studied. In the first case the walls have been fixed at the experimental chamber wall temperature at the last chamber wall axial coordinate (ISOT). In the second case an adiabatic condition has been assumed (ADIAB).
- Chamber outer walls: imposed heat losses considering an air temperature of 290 K (the same as the initial temperature of the solid) and an arbitrary convective heat transfer coefficient of 10 W/(m^2· K) (in accordance with [47]).

A summary of the boundary conditions is given in Fig. 22. The whole three seconds of the experiment have been simulated.

In order to compare the temperature field in the solid with the data recorded in the experiment, the axial evolution of temperature at the position of the first row of thermocouples has been extracted. The thermocouples are installed along the chamber axis at a distance of 1 mm from the chamber walls (see Fig. 22). The temperature field extracted from the numerical simulation has been averaged during 0.5 s, starting 2 s after the beginning of the run, exactly as in the experiment. Results are shown in Fig. 24. The agreement is excellent up to an axial coordinate x = 120 mm, corresponding to the good prediction of wall heat flux by the LES. At higher axial coordinates the temperature is underestimated, as was the heat flux. Results also reveal the influence of the boundary condition on the nozzle walls. An influence of the boundary condition is visible also at the injector side, even if it is of smaller amount.

The good results on the temperature in the first half of the chamber permit to cross-validate the LES methodology and give confidence with regards to the results obtained.

In order to illustrate the three-dimensional character of the temperature field in the solid a longitudinal and transverse cut (at x = 120 mm) of the chamber wall are presented in Fig. 25. The fields correspond to a simulation time of 2.5 s, i.e., the end of the averaging time for the temperature axial evolution of Fig. 24.

Focusing specifically on the transverse cut (top of Fig. 25), one can notice how the temperature field in the combustion chamber wall assumes a quasi-round

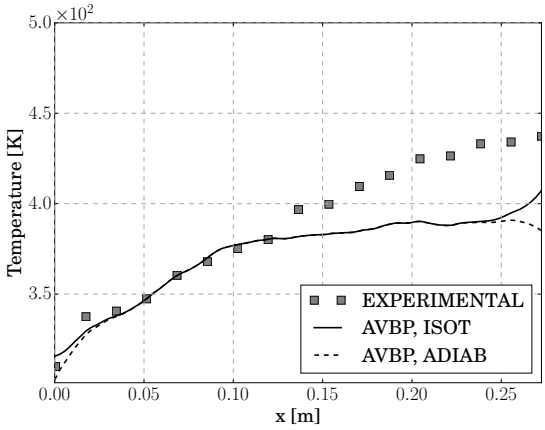

Fig. 24: Solid structure temperature evolution at 1 mm from the chamber walls

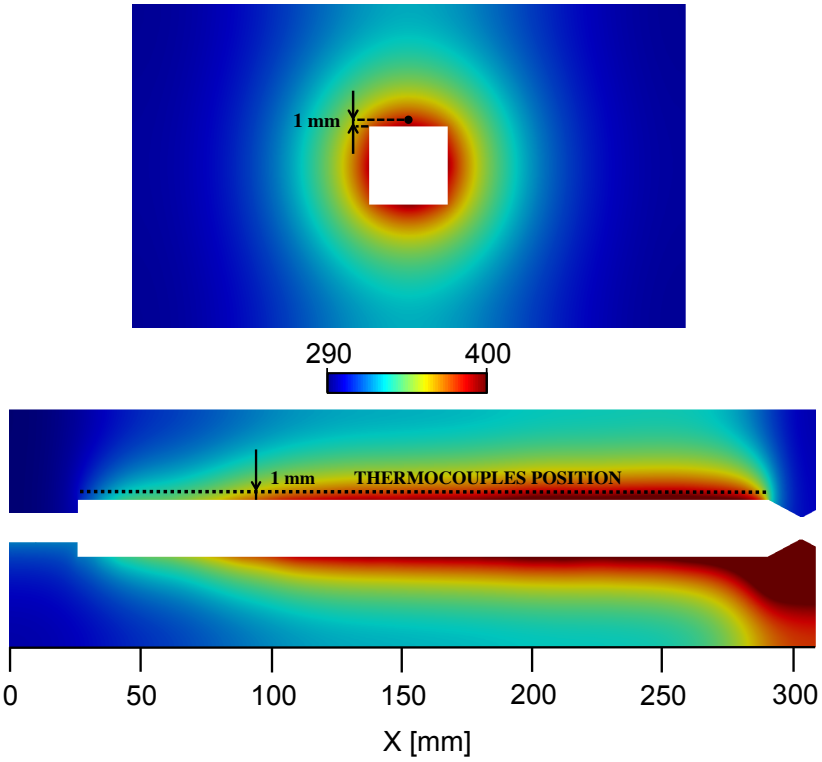

Fig. 25: Temperature field in the chamber wall. Top row: transverse cut at x = 120 mm. Bottom row, top half: longitudinal cut with adiabatic injector, faceplate and nozzle walls (ADIAB case). Bottom row, bottom half: longitudinal cut with isothermal injector, faceplate and nozzle walls (ISOT case).

shape, coherent with the heat flux distribution of Fig. 23. A slight sign of preferential heat diffusion in the directions where the external walls are closer is visible.

Analyzing the circumferential distribution of solid temperature on the inner chamber walls, one can quantify the impact of imposing a circumferentially constant value of temperature in the LES. Figure 26 shows the temperature profile on one side of the inner chamber wall, from edge to edge. The wall temperature varies

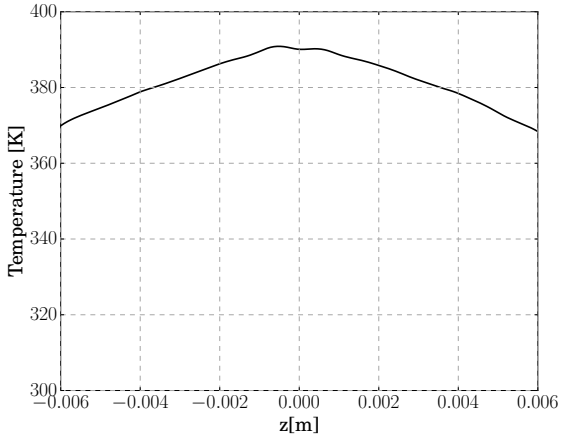

Fig. 26: Solid structure temperature evolution on one side of the inner chamber walls.

between 370 K at chamber edges and 390 K at the chamber center. Considering a circumferentially constant temperature, the error introduced is not of leading order.
Moreover, the difference between the wall temperature from AVTP and the one evaluated at TUM can be quantified here. TUM used the thermocouples data and their in-house tool Thermtest [48] to extrapolate the chamber wall temperature. We focus on the location x = 120 mm, a position at which the experiment and numerical simulation provide the same wall heat flux and thermocouple temperature. Here, the temperature predicted by Thermtest at the chamber center is of about 410 K, i.e., 20 K higher than the one predicted using AVTP.

6 Conclusions

A single element GCH_4/GOx rocket combustion chamber has been computed using Large Eddy Simulation.

The flow and flame structures in the near injector flow field have been studied and a comparison with experimental visualizations of the flame has been provided, showing a good agreement in terms of flame shape and evolution. The overall flame structure has also been analyzed. The analysis showed a purely strained diffusion flame which closes at nearly two thirds of the chamber length. The flame rarely touches the walls and pockets of burning gases intermittently cross the nozzle. In the transverse direction the flame shape and the reactants preferential distribution have been highlighted, denoting an octagonal flame shape and a concentration of methane at the chamber edges.

Numerical simulation data in terms of axial pressure and axial wall heat flux evolution have been compared to experimental data, showing a good agreement. It has been found an influence of leading order of the interaction between the wall law and the sub-grid scale model used for turbulent viscosity. An energy balance to explain the contribution of heat release rate and heat losses at walls to the pressure evolution has been developed.

Finally, a thermally chained numerical simulation of the heat conduction in the chamber structure has been performed in order to cross-validate the heat flux evaluation with regards to the temperature measured in the solid structure during the hot firing tests. Results showed an excellent agreement in the zones in which the wall heat flux was well predicted. This gives strength to the LES results and permits to label the methodology used as reliable for wall heat flux evaluations.

Differences in terms of wall heat flux evaluation and chamber structure temperature have been found in the second half of the combustion chamber and further work is necessary in order to improve the prediction in this zones.

Funding and conflict of interest

Funding: this work has been funded by CERFACS in the context of D. Maestro PhD work. The numerical simulations presented in the paper have been performed using HPC resources provided by CINES of GENCI under the allocations A0032B10157 and A0012B07036.
Conflict of interest: the authors declare that they have no conflict of interest.

References

1. H. Burkhardt, M. Sippel, A. Herbertz, J. Klevanski, Journal of Spacecraft and Rockets **41**(5), 762 (2004)
2. D. Preclik, G. Hagemann, O. Knab, C. Mading, D. Haeseler, O. Haidn, A. Woschnak, M. DeRosa, in *41st AIAA/ASME/SAE/ASEE Joint Propulsion Conference & Exhibit* (2005)
3. K. Liang, B. Yang, Z. Zhang, Journal of Propulsion and Power **14**(5) (1998)
4. A. Fröhlich, M. Popp, G. Schmidt, D. Thelemann, in *Joint Propulsion Conference and Exhibit* (1993)
5. L. Vingert, M. Habiballah, P. Vuillermoz, in *4th International Conference on Launcher Technology "Space Launcher Liquid Propulsion", Liège, Belgium* (2002), p. 77
6. F. Cuoco, B. Yang, M. Oschwald, in *24th International Symposium on Space Technology and Science* (2004)
7. M.P. Celano, S. Silvestri, G. Schlieben, C. Kirchberger, O.J. Haidn, T. Dawson, R. Ranjan, S. Menon, in *SP-2014-2969417* (2014)
8. C. Roth, O. Haidn, H. Riedmann, B. Ivancic, D. Maestro, B. Cuenot, L. Selle, Y. Daimon, A. Chemnitz, R. Keller, et al., Proceedings of the 2015 Summer Program (2015)
9. D. Maestro, L. Selle, B. Cuenot, Proceedings of the 2015 Summer Program (2015)
10. C. Roth, O. Haidn, A. Chemnitz, T. Sattelmayer, G. Frank, H. Müller, J. Zips, R. Keller, P. Gerlinger, D. Maestro, L. Selle, B. Cuenot, H. Riedmann, in *52nd AIAA/SAE/ASEE Joint Propulsion Conference* (2016)
11. D. Maestro, B. Cuenot, A. Chemnitz, T. Sattelmayer, C. Roth, O. Haidn, Y. Daimon, R. Keller, P.M. Gerlinger, G. Frank, et al., in *52nd AIAA/SAE/ASEE Joint Propulsion Conference* (2016)
12. H. Müller, J. Zips, M. Pfitzner, D. Maestro, B. Cuenot, S. Menon, R. Ranjan, P. Tudisco, L. Selle, in *52nd AIAA/SAE/ASEE Joint Propulsion Conference* (2016)
13. D. Maestro, B. Cuenot, L. Selle, in *7th European Conference for Aeronautics and Space Sciences (EUCASS)* (2017)

14. M.P. Celano, S. Silvestri, G. Schlieben, C. Kirchberger, O.J. Haidn, in *5th European Conference For Aeronautics And Space Sciences (EUCASS)* (2013)
15. M. Celano, S. Silvestri, J. Pauw, N. Perakis, F. Schily, D. Suslov, O.J. Haidn, in *6th European Conference of Aeronautics and Space Science, Krakow, Poland* (2015)
16. R. Sankaran, E. Hawkes, J. Chen, T. Lu, C. Law, Proceedings of the combustion institute **31**(1), 1291 (2007)
17. T. Lu, C. Law, Proceedings of the Combustion Institute **30**(1), 1333 (2005)
18. T. Lu, Y. Ju, C. Law, Combustion and Flame **126**(1), 1445 (2001)
19. M. Frenklach, H. Wang, M. Goldenberg, G. Smith, D. Golden, Gri-mech: An optimized detailed chemical reaction mechanism for methane combustion. topical report, september 1992-august 1995. Tech. rep., SRI International, Menlo Park, CA (United States) (1995)
20. R. Mari, Influence of heat transfer on high pressure flame structure and stabilization in liquid rocket engines. Ph.D. thesis (2015)
21. D. Goodwin, H.K. Moffat, R. Speth, Caltech, Pasadena, CA (2009)
22. R. Bilger, S. Staarner, R. Kee, Combustion and Flame **80**(2), 135 (1990)
23. T. Poinsot, S. Lele, J. Comput. Phys. **101**(1), 104 (1992)
24. Y. Daimon, H. Terashimay, N. H., O. Haidn, Proceedings of the 2015 Summer Program (2015)
25. O. Cabrit, Modelisation des flux parietaux sur les tuyeres des moteurs a propergol solide. Ph.D. thesis (2009)
26. W. Kays, M. Crawford, B. Weigand, *Convective heat and mass transfer* (McGraw-Hill Inc., New York, 2004)
27. W.H. Press, B.P. Flannery, S.A. Teukolsky, W.T. Vetterling, *Numerical recipes: The art of scientific computing* (Cambridge U. Press, Cambridge, MA, 1986)
28. T. Schønfeld, M. Rudgyard, AIAA Journal **37**(11), 1378 (1999)
29. N. Gourdain, L. Gicquel, G. Staffelbach, O. Vermorel, F. Duchaine, J.F. Boussuge, T. Poinsot, Comput. Sci. Disc. **2**(1), 28pp (2009)
30. P.D. Lax, B. Wendroff, Commun. Pure Appl. Math. **13**, 217 (1960)
31. F. Nicoud, H. Baya Toda, O. Cabrit, S. Bose, J. Lee, Phys. Fluids **23**(8), 085106 (2011)
32. S. Chapman, T.G. Cowling, *The mathematical theory of non-uniform gases: an account of the kinetic theory of viscosity, thermal conduction and diffusion in gases* (Cambridge university press, 1970)
33. C.R. Wilke, The journal of chemical physics **18**(4), 517 (1950)
34. J.P. Legier, T. Poinsot, D. Veynante, in *Proc. of the summer program* (2000), pp. 157–168
35. F. Shum-Kivan, Simulation des grandes echelles de flammes de spray et modélisation de la combustion non-prémélangée. Ph.D. thesis, Institut National Polytechnique de Toulouse (2017)
36. B. Cuenot, T. Poinsot, Direct Numerical Simulation for Turbulent Reacting Flows p. 225 (1996)
37. F. Charlette, C. Meneveau, D. Veynante, Combustion and Flame **131**(1), 159 (2002)
38. O. Colin, F. Ducros, D. Veynante, T. Poinsot, Physics of Fluids **12**(7), 1843 (2000)
39. F. Winter, S. Silvestri, M.P. Celano, G. Schlieben, O. Haidn, in *European Conference for Aeronautics and Space Sciences* (2017)
40. J. Smagorinsky, Monthly weather review **91**(3), 99 (1963)
41. M. Rudgyard, T. Schönfeld, I. D'Ast, in *International Conference on High-Performance Computing and Networking* (Springer, 1996), pp. 358–364
42. L. Potier, Large eddy simulation of the combustion and heat transfer in sub-critical rocket engines. Ph.D. thesis, Institut National Polytechnique de Toulouse (2018)
43. T. Poinsot, D. Veynante, *Theoretical and numerical combustion* (RT Edwards, Inc., 2012)
44. F. Duchaine, S. Mendez, F. Nicoud, A. Corpron, V. Moureau, T. Poinsot, Comptes-rendus de l'Académie des sciences. Série IIb, Mécanique **337(6-7)**, 550 (2009)
45. J. Donea, A. Huerta, *Finite element methods for flow problems* (John Wiley & Sons, 2003)
46. V. Frayssé, L. Giraud, S. Gratton, J. Langou, CERFACS, Toulouse Cedex, France, Tech. Rep. TR/PA/97/49,[Online]. Available: www. cerfacs. fr (1997)
47. N. Perakis, M.P. Celano, O.J. Haidn, in *7th European Conference for Aerospace Sciences* (2017)
48. C. Kirchberger, G. Schlieben, O.J. Haidn, in *49th AIAA/ASME/SAE/ASEE Joint Propulsion Conference* (2013), p. 4144